Finitte-Difference Time-Domain Studies on Optical Transmission through Planar Nano-Apertures in a Metal Film

Eric X. JIN and Xianfan XU*

School of Mechanical Engineering, Purdue University, West Lafayette, IN 47907, USA

The finite-difference time-domain (FDTD) method is employed to numerically study the transmission characteristics of an H-shaped nano-aperture in a metal film in the optical frequency range. It is demonstrated that the fundamental TE_{10} mode concentrated in the gap between the two ridges of the H-shaped aperture provides a high transmission efficiency above unity and the size of the gap determines the sub-wavelength resolution. Fabry–Perot-like resonance is observed. Localized surface plasmon (LSP) is excited on the edges of the aperture in a silver film but has a negative effect on the signal contrast and field concentration, while aluminum acts similar to an ideal conductor if the film thickness is several times larger than the finite skin depth. In addition, it is shown that two other ridged apertures, C-shaped and bowtie-shaped apertures, can also be used to achieve a sub-wavelength resolution in the near field with a transmission efficiency above unity and a high contrast. [DOI: 10.1143/JJAP.43.407]

1. Introduction

Since it was first proposed by Synge[1] in as early as 1928, sub-wavelength apertures have been employed to obtain sub-wavelength light spots. These sub-wavelength light sources have found their applications in scanning near field optical microscopy (SNOM), and potentially for optical data storage, nano-lithography, bio-chemical sensing, and many other areas where super optical resolution is needed. Although the resolution is only determined by the size of sub-wavelength apertures and no longer limited by diffraction, the drawback of sub-wavelength apertures is somehow inevitable according to the earlier theoretical work.[2–5] In a regular sub-wavelength apertures (circular or square), light throughput is proportional to the fourth power of the aperture size, thus large input powers are necessary for signal generation. Recently, a number of novel designs of planar nano-apertures[6–10] have been reported to obtain the nanoscale resolution and high power throughput simultaneously. One strategy is to take advantage of the enhancement of localized surface plasmon (LSP) by introducing a minute scatter in the center of a regular aperture.[6] Another is to design shapes of the aperture other than circular or square to achieve high throughput.[7–10] Results of numerical simulations of a C-shaped aperture[7] made in a perfect conducting metal film is found to have an enhanced performance of power throughput compared with a square aperture. The mechanism of enhancement of power throughput from C-shaped aperture is explained as the propagation of the dominant TE_{10} mode, analogous to the ridged waveguide in microwave engineering. A T-shaped aperture[8] is proposed to provide continuous signal of readout data and tracking error for near-field surface recording. Bowtie slot antennas and regular apertures in gold and silver films are compared at optical frequencies in terms of the field response and the focused spot size.[9] An I-shaped sub-wavelength aperture[10] in a thick silver screen is also examined. The high-intensity emission and the ultra-small spot size are explained[9,10] as the result of the surface plasmon excitation. All these works are conducted numerically using the finite-difference time-domain (FDTD) method.[11–13] In addition to the apertures on a surface (planar apertures), there is a larger amount of numerical work using FDTD for analyzing the SNOM,[14–16] for designing SNOM probes, for examples, apertureless probes,[17] double-tapered optical fiber probes,[18] and silicon dioxide atomic force microscopy (AFM) probes,[19] for investigating near-field aperture solid immersion lens probes,[20,21] and for designing optical head for hybrid data recording.[22,23]

The focus of this work is on the apertures with a planar structure. The C-shaped, bowtie-shaped (or bowtie slot antenna), and I-shaped apertures mentioned above have one feature in common, the small gap region formed by the ridge or ridges, which is the key structure for providing the high optical transmission efficiency and the sub-wavelength spot size. In this work, we named them ridged apertures, and a systematic study is conducted on optical transmission on these apertures. In order to fully understand the optical transmission properties of these ridged apertures, we select the H-shaped (similar to I-shaped) aperture for detailed theoretical and numerical analysis to take advantage of the waveguide theory in microwave engineering. Other ridged apertures are also studied and compared with the results of the H-shaped apertures.

In the following text, the simulation model is presented first. The cutoff property of the H-shaped aperture is then studied by considering it as a short double-ridged waveguide channel. By performing FDTD simulations, the full wave 3-D electromagnetic fields inside and in the near-field regions of the aperture are obtained to illustrate its optical transmission characteristics. Ideal conductor is considered to reveal some basic transmission characteristics of the H-shaped aperture. For thin metal films, the modified Debye model[12] is used to simulate the behavior of real metal (aluminum and silver). With the use of optical properties of real metal, it is also possible to analyze the effect of surface plasmon. Finally, three ridged apertures of different shapes, H-shaped aperture (double-ridged), C-shaped aperture (single-ridged), and bowtie-shaped aperture (gradually double-

---
*To whom correspondence should be addressed.
 E-mail address: xxu@ecn.purdue.edu

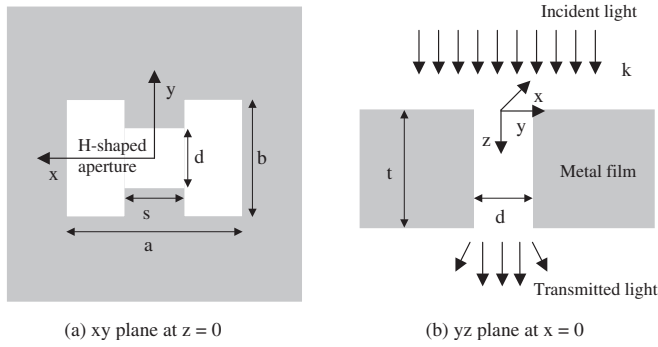(a) xy plane at z = 0   (b) yz plane at x = 0

Fig. 1. Schematic view of an H-shaped nanoscale aperture channel in a free-standing metal film. The normal incident light to be considered is monochromatic and linearly polarized along the y-direction.

ridged) are compared in terms of transmission efficiency, field distribution, signal contrast, spot size, and shape. It turns out that all three apertures can be used to achieve high transmission efficiency as well as nanoscale resolution in a wide optical frequency range. Light passes through these apertures due to the key propagation TE_{10} mode, which is concentrated in the gap region of these apertures. The nanoscale resolution can be obtained by defining the smallest feature size, usually the gap between ridges, of these apertures.

2. Simulation Model

Figure 1 illustrates the cross-sectional views of the structure of interest on *xy* and *yz* planes. An H-shaped nanoscale aperture is perforated through a free-standing metal film with a thickness of *t*. The uniform incident field impinges on the metal film in the normal direction, with time and distance variations described by $e^{(j\omega t - \gamma z)}$.

The Maxwell's differential equations for the light propagation are:

$$\nabla \times \boldsymbol{E} + \mu_0 \frac{\partial \boldsymbol{H}}{\partial t} = 0 \quad (1a)$$

$$\nabla \times \boldsymbol{H} - \frac{\partial \boldsymbol{D}}{\partial t} = 0 \quad (1b)$$

$$\boldsymbol{D} = \varepsilon \varepsilon_0 \boldsymbol{E} \quad (1c)$$

Equation (1) is numerically solved with 3D-FDTD method in a simulation volume of $1000 \times 1000 \times 1500$ nm, which is divided into small cubes, the so called Yee cells.[11] The dimension of each cell is chosen to be $5 \times 5 \times 5$ nm to resolve the near field below the aperture. A second-order stabilized Liao[24] absorbing boundary condition is used for the six sides of the simulation volume. The electromagnetic fields are calculated in each cell by solving the discretized Maxwell curl equations in both space and time for each time step until the steady state is reached. In the case of a sinusoidal source as used in this work, the steady state is reached when all scattered fields vary sinusoidally in time. A commercial code, XFDTD 5.3[25] from Remcom, Inc. (State College, PA) is used for the simulation. The time step is 9.63×10^{-18} s, which is determined according to the stability criteria of the FDTD algorithm. The total number of time step is 5000 to sufficiently approach the steady state after monitoring the

fields at a point 100 nm below the aperture.

At optical frequencies, real metals, such as aluminum and silver, have complex permittivities which are strongly dependent on the excitation frequency. In order to treat real metals accurately, a modified Debye model[12] is used to describe the frequency dependence of the complex relative permittivity, which is given by,

$$\tilde{\varepsilon}(\omega) = \varepsilon_\infty + \frac{\varepsilon_s - \varepsilon_\infty}{1 + i\omega\tau} + \frac{\sigma}{i\omega\varepsilon_0} \quad (2)$$

where ε_s represents the static permittivity, ε_∞ is the infinite frequency permittivity which should be no less than 1, σ is conductivity, and τ is the relaxation time. A trial and error method is used to fit these parameters to the experimental values of optical properties, i.e., the complex refractive index. For example, with the experimental data for aluminum at the 488 nm wavelength,[26] it is found that $\varepsilon_s = -640.9549$, $\varepsilon_\infty = 1.0799$, $\sigma = 5.3424 \times 10^6$ S/m, and $\tau = 1.0640 \times 10^{-15}$ s. The values for silver at 488 nm[27] are $\varepsilon_s = -1313.5469$, $\varepsilon_\infty = 1.0220$, $\sigma = 3.7155 \times 10^6$ S/m, and $\tau = 3.1326 \times 10^{-15}$ s.

3. Results and Discussion

First, the cutoff properties of waveguides are studied in order to understand the transmission efficiency and light concentration of the H-shaped aperture. This will be illustrated further by comparing results from FDTD simulations to the results of regular apertures. In addition, the electric dipole-liked behavior and transmission resonance of the H-shaped aperture will be discussed. Surface plasmon and finite skin depth effects will also be studied using real metal properties described above. At last, results of three ridged apertures of different aperture shapes will be compared.

3.1 H-shaped aperture in an ideal conductor film

The H-shaped aperture channel can be approximated as a short double-ridged waveguide if an ideal conductor film is considered and the aperture end effect is negligible. Here a conductor film with thickness $t = 500$ nm is considered which is much larger than the skin depth of a metal. Considering the incident excitation given in the last section, the wave equation can be reduced to the Helmholtz formulation,[28] and the property of the wave inside the waveguide is described by the propagation constant γ ($= j\beta$, where β is phase constant). By introducing the cutoff number k_c, the wave propagation constant is completely determined by

$$k_c^2 = \gamma^2 + k^2 \quad \text{or} \quad \gamma^2 = \left(\frac{2\pi}{\lambda_c}\right)^2 - \left(\frac{2\pi}{\lambda}\right)^2 \quad (3)$$

For incident light with a wavelength shorter than the cutoff wavelength λ_c, it can propagate through the aperture channel, as the phase constant β is positive. The group wavelength inside the channel is related to the phase constant β by $\lambda_g = 2\pi/\beta$. The cutoff wavelength of double-ridged waveguide for TE_{m0} modes can be derived using the transverse resonance method,[29] which are the eigenvalues of the following equation:
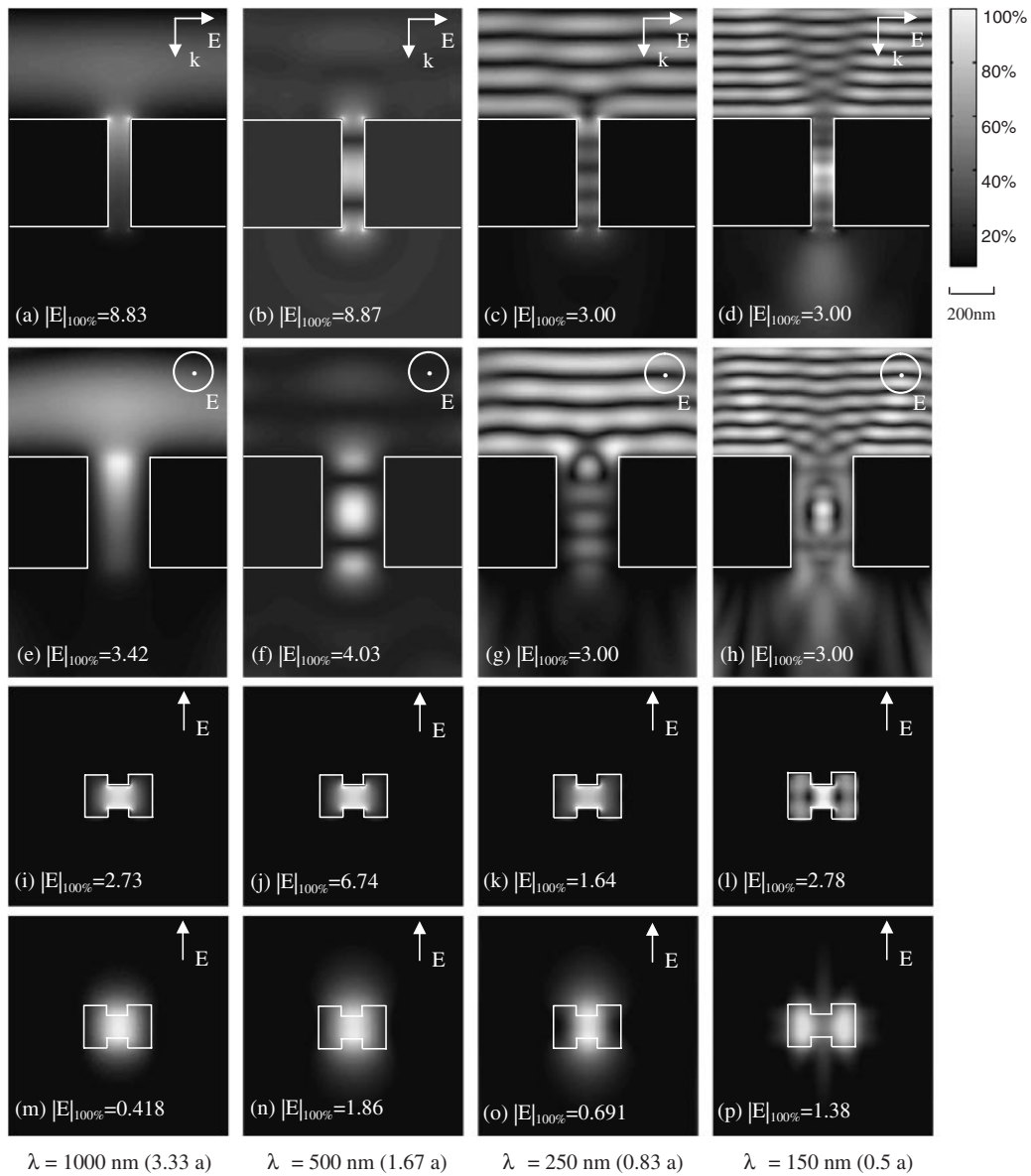
Fig. 2. Distribution of the maximum electric field amplitude $|E|$ of H-shaped aperture ($a = 300$ nm, $b = 200$ nm, $s = 100$ nm, $d = 100$ nm) in an ideal conductor film of 500 nm thick illuminated by y-polarized incident plane wave of different wavelengths, on yz plane at $x = 0$, xz plane at $y = 0$, xy plane cutting through the middle of the film, and xy plane 50 nm behind the aperture, from the first row to fourth row respectively. From the first column to fourth column, the wavelength is 1000 nm, 500 nm, 250 nm and 150 nm, respectively. The peak amplitudes are shown as the insets of each plot taking the amplitude of incident electric field to be 1.

$$-\cot\left(\frac{\pi(a-s)}{\lambda_c}\right) + \frac{b}{d}\tan\left(\frac{\pi s}{\lambda_c}\right)$$
$$+ 2\left(\frac{b}{\lambda_c}\right)\ln\left(\operatorname{cosec}\left(\frac{\pi d}{2b}\right)\right) = 0 \qquad (4)$$

where a, b, d, and s are the dimensions of a double-ridged waveguide shown in Fig. 1. Due to the ideal conductor boundary conditions, there is no transverse electromagnetic wave (TEM or TE_{00} mode) that can be supported by a rectangular waveguide or a ridged waveguide. Therefore, the TE_{10} mode is the lowest propagating mode. Given those numerical values in Fig. 1, $a = 300$ nm, $b = 200$ nm, $s = 100$ nm, and $d = 100$ nm, the cutoff wavelength of the fundamental TE_{10} mode is found to be 805 nm, which is $2.68a$ where a is the length of the waveguide.

The maximum amplitude of the electric field $|E|$ at each point in the simulation volume is displayed in Fig. 2.

Different incident wavelengths are investigated. Linearly polarized field along the y-direction is used. It is found that the cutoff frequency of the TE_{01} mode for the H-shaped aperture in Fig. 1 is about 1.4×10^{15} Hz ($\lambda = 214$ nm or $0.71a$), which is much higher than that of the TE_{10} mode, meaning light can pass through the aperture more easily when polarized along the y-direction than the x-direction. In fact, simulation results show that the transmission efficiency, which is evaluated by the ratio of the electric field intensity integrated over the aperture area to incident field intensity integrated over the aperture area, of x-polarized incident light is about 2800 fold less than that of y-polarized incident light. Therefore, the y-direction, the direction across the ridges, is the preferred polarization direction for the H-shaped aperture.

When the incident wavelength is longer than the cutoff wavelength, 805 nm, no propagation mode can exist inside

the aperture channel. This is seen in the case of the 1000 nm wavelength. Only the evanescent wave whose intensity decreases quickly along the z-direction is found, which can be observed from E field distribution on the yz and xz plane [Figs. 2(a) and 2(e)]. When the incident light has a wavelength of 500 nm, shorter than the cutoff wavelength, the fundamental TE_{10} mode is clearly observed in the aperture channel [Figs. 2(b) and 2(f)]. This TE_{10} mode is completely concentrated in the gap region between the ridges as shown in Fig. 2(j) and propagates through the channel without losing much energy. Therefore, a super resolution spot can be found in the near field behind the aperture; and high intensity is obtained [Fig. 2(n)] compared with the case of evanescent wave [Fig. 2(m)]. For an even shorter incident wavelength 150 nm, it is shown in Fig. 2 (the fourth column) that the fundamental mode is not the only excited propagation mode inside the channel. In this case, a TE_{20} mode [Fig. 2(l)] is also excited and propagating along the channel. Further, the field emerging from the channel is no longer concentrated near the gap region, but instead is split into two parts resulting in two light spots in the near-field region below the aperture [Fig. 2(p)]. There-fore, the resolution is reduced. It is noticed that two spots appear near the bottom corners in Fig. 2(h) (similar spots are shown in other figures), which are caused by insufficient boundary absorption there. Since the focus of the calculation is in the near field of the aperture, which is far away from the bottom boundary, it is expected that those spots do not influence the near field results. The calculation result about a 100 nm hole in a thick perfect conducting plate (not shown here) is consistent with results given in the literature,[5] which indicates the validity of the numerical procedures used here.

The broadband property of the ridged waveguide in microwave engineering is also verified here for the H-shaped aperture in the optical frequency range. As shown in the third column in Fig. 2, the previously defined H-shaped aperture also works for ultraviolet frequency, the 250 nm wavelength. In fact, based on the eigenvalue calculation of eq. (4), the spectrum separation between the dominant mode TE_{10} and the first higher order mode is about 580 nm. Therefore, the H-shaped aperture is suited for practical operation as it covers quite a large frequency range instead of a single frequency.

In order to further demonstrate the transmission enhance-ment in the H-shaped aperture, numerical simulations are performed on two regular apertures irradiated by y-polarized 488 nm incident light, a 300×200 nm $(0.61\lambda \times 0.41\lambda)$ rectangular aperture and a 100×100 nm $(0.20\lambda \times 0.20\lambda)$ square aperture, and compared with the 300×200 nm $(0.61\lambda \times 0.41\lambda)$ H-shaped aperture with a gap of 100×100 nm $(0.20\lambda \times 0.20\lambda)$. A 100 nm thick ideal conductor film illuminated by 488 nm wavelength light is considered.

Figure 3 shows distributions of the maximum amplitude of the electric field $|E|$ for the three apertures on the yz plane at $x = 0$, xz plane at $y = 0$, and xy plane at $y = 25$ nm (0.05λ) and 50 nm (0.10λ) behind the apertures. The fundamental cutoff wavelengths, the expected propagation mode inside the aperture, transmission efficiency, the peak value of the electric field at a distance 25 nm (0.05λ) behind the apertures, the spot size which is the full width half magnitude (FWHM) of electric field intensity at a distance

25 nm (0.05λ) behind the apertures along x and y directions, and signal contrast defined as $(I_{max} - I_{min})/(I_{max} + I_{min})$ at a distance 50 nm (0.10λ) behind the apertures are summarized in Table I.

No propagating wave front can be found inside the square aperture as its cutoff wavelength 200 nm is far below that of the incident wave. As expected, the electromagnetic field becomes very weak below the aperture (the third column in Fig. 3). On the other hand, the TE_{10} propagation mode is found for both the H-shaped and the rectangular apertures since the incident wavelength is below their cutoff wave-lengths, 805 nm and 600 nm, respectively.

Although a small spot is formed below the square aperture [Fig. 3(i)] due to the evanescent wave through the aperture channel, the transmission efficiency is as low as 0.0038. In contrary, the optical transmission efficiency through the H-shaped aperture is 2.14, which is higher than 1 and is about a 563 fold enhancement over the square aperture. It is also evident from Fig. 3(l) that the contrast of the signal coming out from the small square aperture is too low to be distinguished from the background at a distance 50 nm (0.10λ) below the aperture. Compared with the rectangular aperture, the spot size for the H-shaped aperture shrinks in both x and y directions, while their transmission efficiencies, peak field intensities, and signal contrasts are comparable.

A close look at the field distributions of the H-shaped aperture reveals that it resembles an electric dipole. Figures 4(a) and 4(b) show the dB scaled distributions of maximum amplitudes of $|E|$ and $|B|$ on the yz plane at $x = 0$ for the H-shaped aperture. The isolines of both electric and magnetic fields are half-circles centered on the aperture. The electric field decreases more rapidly away from the aperture than the magnetic field, which can be observed in the $|E|$ and $|B|$ variation along $y = 0$ line on the yz plane (Fig. 5). This kind of field behavior is the same as that of an electric dipole in the near-field region.[28] Furthermore, the profile of power densities on the plane right behind the H-shaped aperture in Fig. 6 shows that the total power density is dominated by the electric field in the near-field region of the aperture. In contrast, for the square aperture, the power density is dominated by the magnetic field as shown in Fig. 7, which corresponds to a magnetic dipole predicted by Bethe.[2] It is noticed that the scale of Fig. 6 is 2 or 3 orders higher than that of Fig. 7, which further confirms the transmission enhancement of the H-shaped aperture. The two peaks of electric power density $(\varepsilon_0|E|^2/2)$ on the rims of both apertures in the y-direction (the direction of incident polarization) arise from the accumulated high surface charge density on the edges. The local electric power density there enhance to a factor of 4 compared with the center for both apertures. In the x-direction, the central peak of the electric power density is enclosed by two peaks of the magnetic one, as the magnetic field always curls around the axis of the electric dipole.[28] The electric dipole-liked behavior is another advantage of ridged aperture over the regular apertures for near-field optical applications since the interaction between visible light and matter is dominated by the electric field. The transmitted electromagnetic energies are stored in the near field of the aperture. In the z-direction, the electric field decays more than half in a distance of 200 nm (0.41λ). The FWHMs of the electric
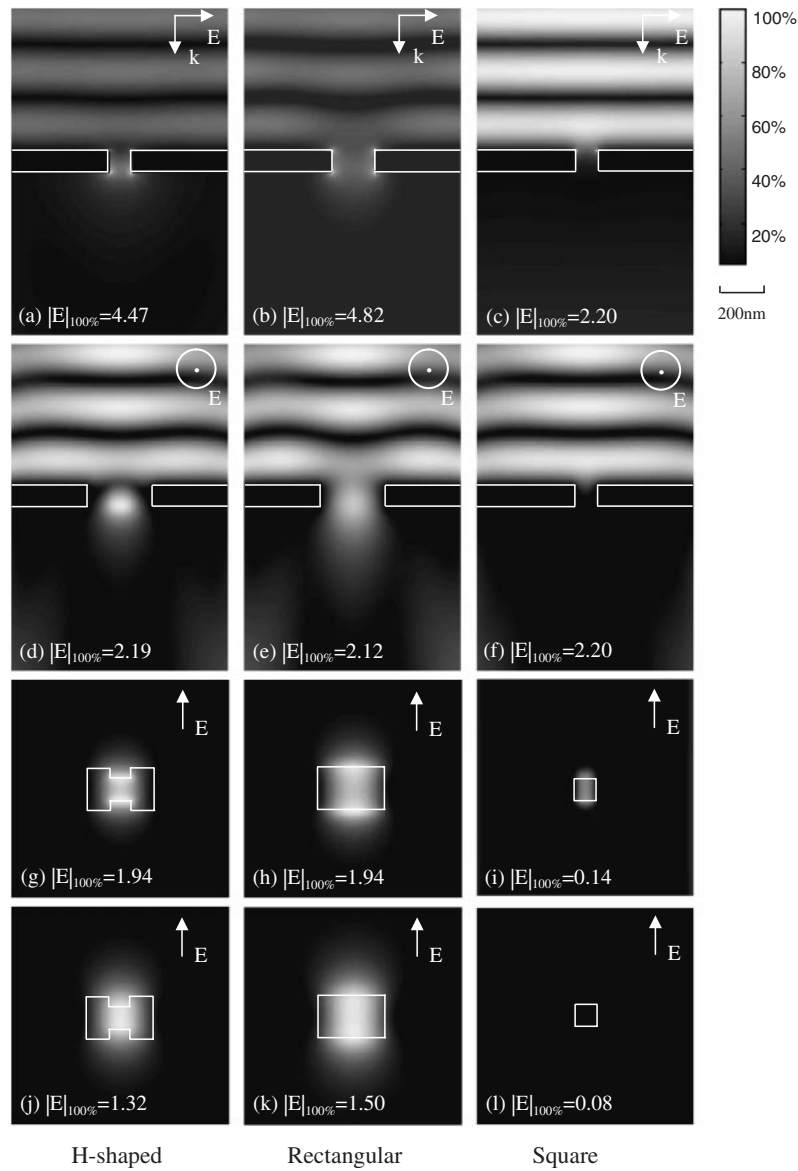
Fig. 3.   Distribution of the maximum electric field amplitude $|E|$ of nano-apertures of different shapes in a 100 nm (0.20λ) thick ideal conductor film. From the first column to third column, the aperture is 300×200 nm ($0.61 \times 0.41\lambda$) H-shaped with a gap 100×100 nm ($0.20 \times 0.20\lambda$), 300×200 nm ($0.61 \times 0.41\lambda$) rectangular and 100 nm (0.20λ) square, respectively. The first row to fourth row shows yz plane at $x = 0$, xz plane at $y = 0$, xy planes 25 nm (0.05λ) and 50 nm (0.10λ) behind the aperture, respectively. y-polarized, 488 nm normally incident light is considered for all cases. The peak amplitudes are shown as the insets of each plot. The amplitude of the incident electric field is 1.

Table I.   Comparison of H-shaped, rectangular and square apertures.

	H-shaped aperture	Rectangular aperture	Square aperture
Aperture dimensions	300×200 nm ($0.61 \times 0.41\lambda$)	300×200 nm ($0.61 \times 0.41\lambda$)	100 nm (0.20λ)
Gap size	100×100 nm ($0.20 \times 0.20\lambda$)	NA	NA
Fundamental cutoff wavelength (nm)	805	600	200
Existing propagation mode	TE_{10}	TE_{10}	No
Transmission efficiency	2.14	2.31	0.0038
$|E|_{max}$ at $d = 25$ nm (0.05λ)	1.84	1.86	0.039
Spot size at $d = 25$ nm (0.05λ)	130×168 nm ($0.27 \times 0.34\lambda$)	168×262 nm ($0.34 \times 0.54\lambda$)	60×140 nm ($0.12 \times 0.28\lambda$)
Signal contrast at $d = 50$ nm (0.10λ)	0.770	0.823	NA[a]

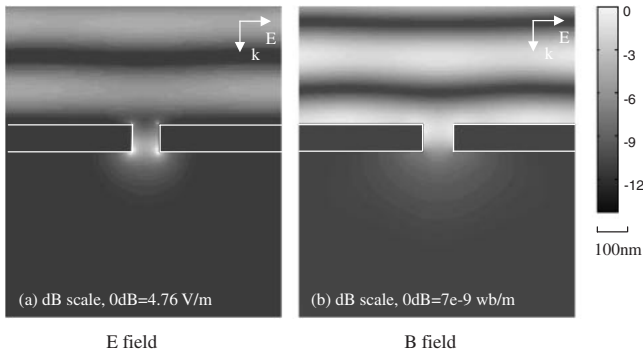a) The output signal can not be distinguished with the background as seen in Fig. 3(l).

Fig. 4. dB scaled distributions of field maximum amplitudes |E| and |B| for the H-shaped aperture in a 100 nm thick ideal conductor film on yz plane at x = 0. The amplitude of the incident electric field is 1.
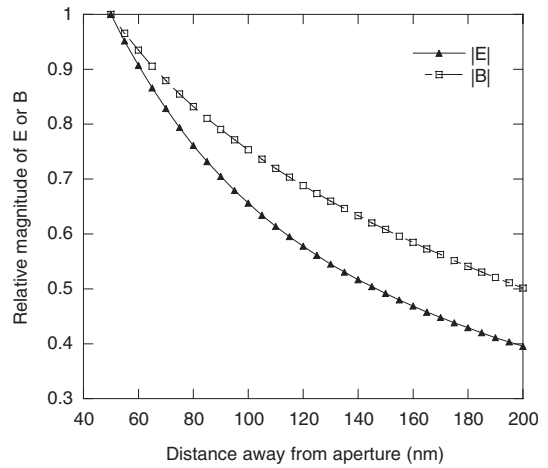

Fig. 5. Variations of maximum amplitudes |E| and |B| along y = 0 on the yz plane behind the H-shaped aperture in a 100 nm thick ideal conductor film.
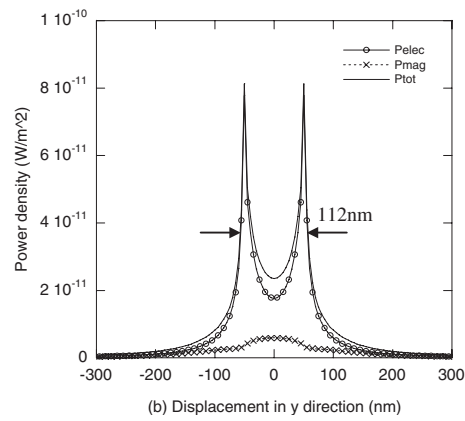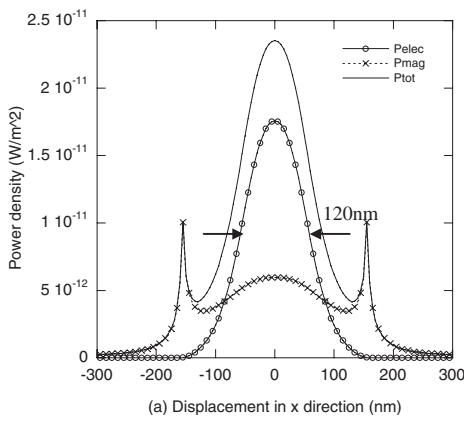

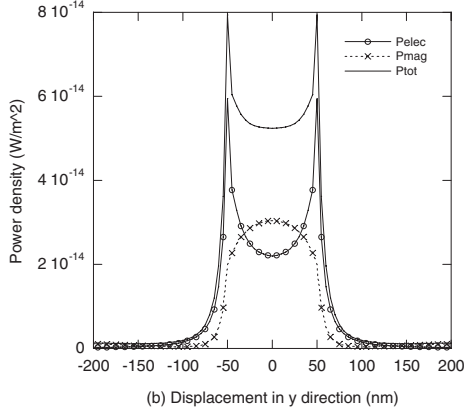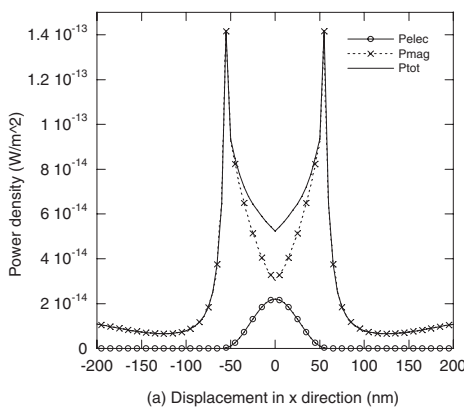Fig. 6. Power density profiles on the plane right behind the H-shaped aperture in x and y directions.

Fig. 7. Power density profiles on the plane right behind the 100×100 nm ($0.20 \times 0.20\lambda$) square aperture in a 100 nm (0.20λ) thick ideal conductor film in x and y directions.

power density in the x- and y-directions are 120 nm (0.25λ) and 112 nm (0.23λ), respectively (Fig. 6), approximately corresponding to the gap size. Power densities decay exponentially both in x- and y-directions, and become almost zero at the displacements of 200 nm (0.41λ). Similar results can be observed for the square aperture (Fig. 7).

To further investigate the transmission behavior of the H-

shaped aperture, its spectral variation and dependence on the film thickness are calculated. Several transmission peaks are found in the transmission spectrum in a 500 nm thick ideal conductor film as shown in Fig. 8. Conversely, transmission peaks are also found at some particular thicknesses when the incident wavelength is held constant as shown in Fig. 9. It has been reported that in narrow slits,[30–32] a Fabry–Perot-
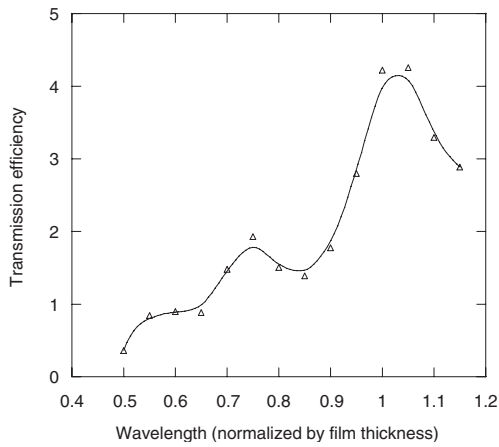
Fig. 8. Transmission spectrum of the H-shaped aperture in 500 nm thick ideal conductor film. Uniform y-polarized plane wave is normally incident on the top surface of the film.
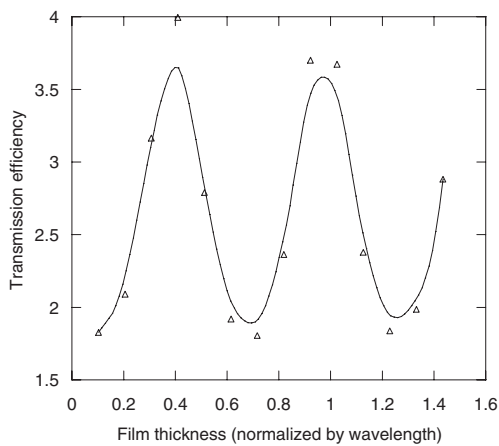

Fig. 9. Transmission efficiency through the H-shaped aperture in a thick ideal conductor film of different thickness under 488 nm y-polarized illumination.

like resonance will occur for a single narrow slit in a perfect conductor. Similar resonance is also found for the H-shaped aperture discussed here. The Fabry–Perot resonance follows the condition[30]

$$\frac{m}{2}\lambda_g = t \tag{5}$$

where t is the length of the Fabry–Perot cavity, and equals to the film thickness here. With eqs. (5) and (3), the resonant incident wavelengths λ can be estimated. In our case, they are found to be 239 nm ($0.48t$), 308 nm ($0.62t$), and 425 nm ($0.85t$) in the wavelength range of interest. Compared with FDTD simulation results in Fig. 8, the resonance wavelengths shift towards longer wavelengths, 275 nm ($0.55t$), 375 nm ($0.75t$), and 520 nm ($1.04t$) respectively. This wavelength shift is caused by the finite length of the aperture channel (film thickness). As noted in the description of eq. (3), eq. (3) is valid for aperture waveguide with infinite length. Therefore, results estimated using eqs. (5) and (3) do not match with the FDTD results exactly. Results in Figs. 8 and 9 show how to choose the wavelength or the film thickness in order to optimize the transmission efficiency through a nano-aperture.

3.2 Effects of surface plasmon and finite skin depth

So far, only ideal conductor films are considered. For applications involving very thin films, the effect of real metals needs to be examined. Figure 10 compares maximum amplitude of the electric field $|E|$ in the vicinity of identical H-shaped apertures ($a = 300$ nm, $b = 120$ nm, $s = 100$ nm and $d = 50$ nm) in a film of equal thickness $t = 50$ nm, made of ideal conductor (IC), aluminum, and silver, respectively, at an incident wavelength of 488 nm. At this wavelength, most real metals have complex dielectric constants, which are $-34.80 + 8.73i$ for aluminum and $-7.90 + 0.74i$ for silver.

In the IC case, the transmitted electric field approaches zero on the film surface, which is consistent with the boundary condition for an ideal conductor. As a conse-
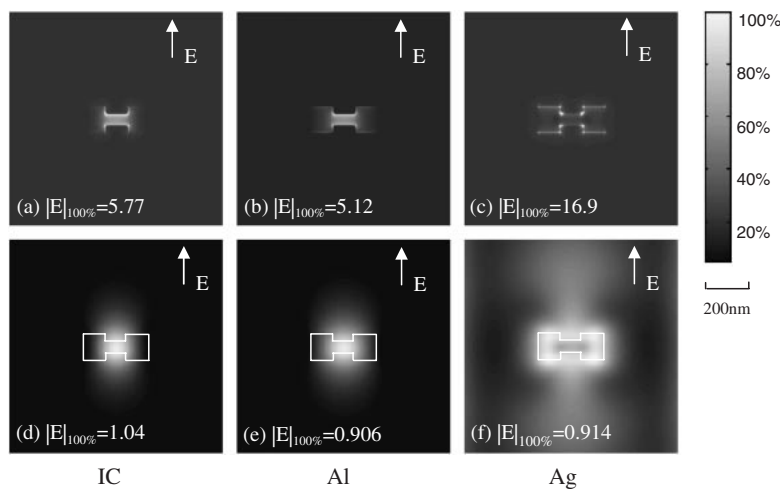

Fig. 10. Distribution of the maximum electric field amplitude $|E|$ of an H-shaped aperture in a 50 nm (0.10λ) thick ideal conductor, aluminum, and silver film, from the first column to third column, respectively. The aperture is 300×120 nm ($0.61 \times 0.25\lambda$) H-shaped with a gap of 100×50 nm ($0.20 \times 0.10\lambda$). The first and the second row are xy plane right below the film, and the xy plane 50 nm (0.10λ) below the film, respectively. y-polarized 488 nm normally incident light is considered for all cases. The peak amplitudes are shown as the insets in each plot. The amplitude of the incident electric field is 1.

quence, no surface plasmon can be excited. The electric field is confined in the small gap region, which corresponds to the guided waveguide mode as discussed in §3.1. In contrast, the field is locally distributed on the edges of the aperture across the incident polarization direction on the bottom surface of the silver film as seen in Fig. 10(c), which can be attributed to the excitation of the localized surface plasmon[6] (LSP) due to the negative real part of permittivities[33] of both aluminum and silver. A strongly enhanced electric field of a maximum magnitude of 16.9 is observed. The localized surface plasmon excitation is much stronger for Ag than for Al as shown in Figs. 10(c) and 10(b) due to the fact that the absolute value of the ratio of the real part of the complex permittivity to the imaginary part for silver is larger than that for aluminum.[33]

From the calculation, it is also found that the LSP enhances transmission efficiency, which is 2.02, 2.17 and 8.81 for IC, aluminum and silver, respectively. Unlike the transmission enhancement through a hole array in silver film,[34,35] the localized surface plasmon excitation here has a negative effect on the performance of H-shaped aperture. Due to the excited LSP in silver, the field distribution of the transmitted light through the aperture is changed, and the transmitted light does not concentrate in the gap region. Instead, it spreads out quickly along the direction of polarization, enlarges the output spot size and reduces the signal contrast, which can be observed in the Fig. 10(f). In contrary, the output spot in the aluminum as well as the IC case keeps a similar shape. This suggests that 50 nm thick aluminum can be treated as an ideal conduct under 488 nm illumination.

When the film thickness is close to the skin depth of the metal film at the frequency of consideration, some field can transmit through the metallic film. As this field interferes with the field transmitted through the aperture, the concentration of the field in the vicinity of aperture will be disturbed, and the signal contrast will decrease. Figure 11 shows the variation of signal contrast for an aluminum film with thicknesses ranging from 5 nm to 50 nm. The H-shaped aperture considered here has the same geometry used in the last calculation. At 488 nm illumination, the skin depth of aluminum is about 6.5 nm, therefore the low contrast at the film thickness of 5 nm is expected. When the film is thicker
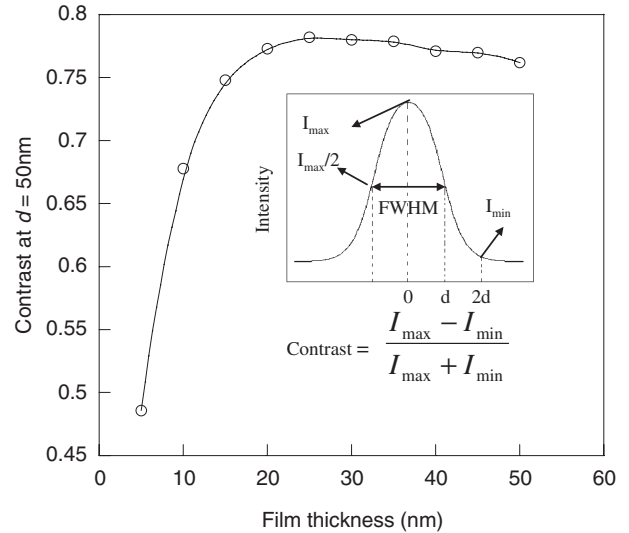

Fig. 11.   Variation of contrast with the thickness of the aluminum film.

than 30 nm, the contrast cannot be improved any more since the peak field intensity I_{max} starts to decrease. This is because as the guided fundamental TE_{10} mode propagates a distance much longer than the skin depth, the energy lost along the side wall of the gap region becomes significant.

3.3 Comparison of different aperture shapes

In this section, three ridged apertures of different shapes, H-shaped, C-shaped and bowtie-shaped, but of equal aperture areas, as well as two comparable regular apertures are compared regarding to the following aspects: electric field intensity distributions, transmission efficiency, peak value of electric field, spot size, and signal contrast. The smallest feature size (gap width) of these apertures is chosen to be 50 nm (0.10λ). A 50 nm-thick aluminum film is illuminated by y-polarized 488 nm uniform incident field for all situations.

Table II compares results of the calculation. In terms of transmission efficiency, electric field intensity and signal contrast, all three apertures show significant advantages over regular apertures. Transmission efficiencies of ridged apertures are all above unity, and signal contrasts are also high compared with the square aperture. It needs to be mentioned

Table II.   Comparison of ridged apertures and regular apertures.

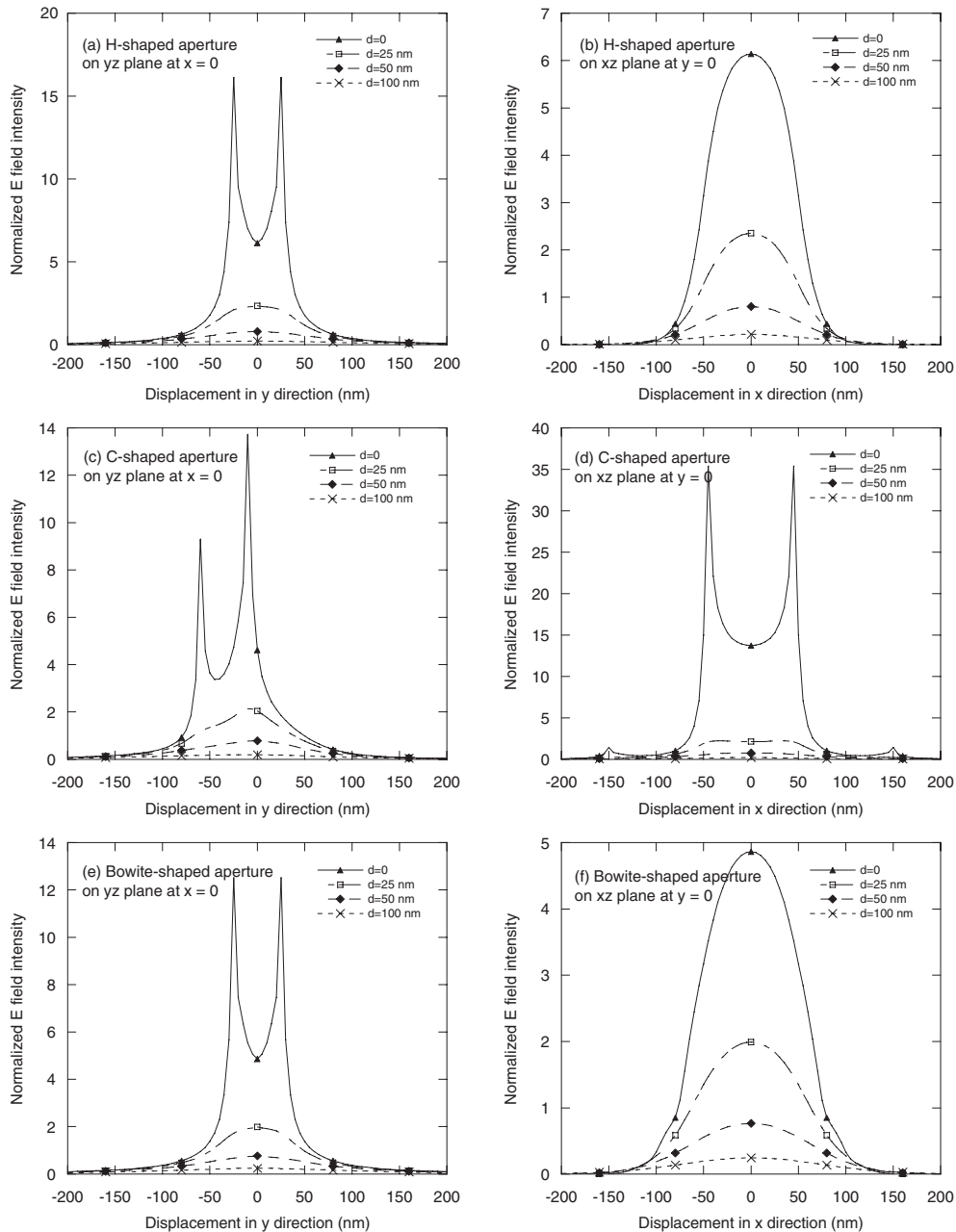|	H-shaped aperture	C-shaped aperture	Bowtie-shaped aperture	Square aperture	Rectangular aperture
Aperture dimensions	300×120 nm ($0.61 \times 0.25\lambda$)	300×120 nm ($0.61 \times 0.25\lambda$)	300×200 nm ($0.61 \times 0.41\lambda$)	100×100 nm ($0.20 \times 0.20\lambda$)	300×100 nm ($0.61 \times 0.20\lambda$)
Gap size	100×50 nm ($0.20 \times 0.10\lambda$)	100×50 nm ($0.20 \times 0.10\lambda$)	100×50 nm ($0.20 \times 0.10\lambda$)	NA	NA
Transmission efficiency	2.023	1.885	1.869	0.856	2.633
$|E|_{max}$ at $d = 25$ nm (0.05λ)	1.60	1.51	1.45	0.664	1.65
Spot size at $d = 25$ nm (0.05λ)	100×96 nm ($0.20 \times 0.20\lambda$)	128×95 nm ($0.26 \times 0.19\lambda$)	122×96 nm ($0.25 \times 0.20\lambda$)	84×148 nm ($0.17 \times 0.30\lambda$)	134×156 nm ($0.27 \times 0.32\lambda$)
Signal contrast at $d = 25$ nm (0.05λ)	0.736	0.714	0.695	0.632	0.752

Fig. 12.   Profiles of normalized electric field intensity along the distance away from three different nano-apertures on yz plane at $x = 0$ and xz plane at $y = 0$. From the first to third row, the aperture is 300×120 nm ($0.61 \times 0.25\lambda$) H-shaped aperture with a 100×50 nm ($0.20 \times 0.10\lambda$) gap, 300×120 nm ($0.61 \times 0.25\lambda$) C-shaped aperture with a 100×50 nm ($0.20 \times 0.10\lambda$) gap, and 300×200 nm ($0.61 \times 0.41\lambda$) bowtie-shaped aperture with a 100×50 nm ($0.20 \times 0.10\lambda$) gap, respectively.

that the transmission efficiency through the square aperture is 0.856 compared with its counterpart listed in Table I, 0.0038. This is because a much thinner aluminum film is considered here and the electromagnetic wave can propagate to some distance along the wall of aluminum film inside the square aperture. Further simulation results show that the transmission efficiency through the square aperture will decrease to 0.017 if the thickness of the aluminum film becomes 150 nm while those through ridges apertures are still above unity. The output spot size in the direction of the gap at $d = 25$ nm is about 96 nm (0.20λ), one third less than that of the comparable rectangular aperture.

Several other common features are also found in the electric field intensity distributions along the direction away from the apertures on yz and xz planes. It is seen in Fig. 12

that the electric field intensity decreases dramatically with the increasing distance d. At about $d = 100$ nm (0.20λ), all profiles become quite flat, meaning the signal contrast is low and the desired signal cannot be well distinguished from the background. The transmitted field through ridged apertures is concentrated in the near-field region behind the apertures as shown in the first two rows in Fig. 13. From the electric field distributions on the xz plane (the second row in Fig. 13) and on the middle of the xy plane inside the film (the third row in Fig. 13), the propagation TE_{10} mode can be found for all three apertures. This TE_{10} mode contributes to the high transmission in all three cases.

On the yz plane at $x = 0$ as shown in the first column in Fig. 12, two peaks of the electric field are found at the rims of the ridges for all three apertures at $d = 0$ [Fig. 12(a),
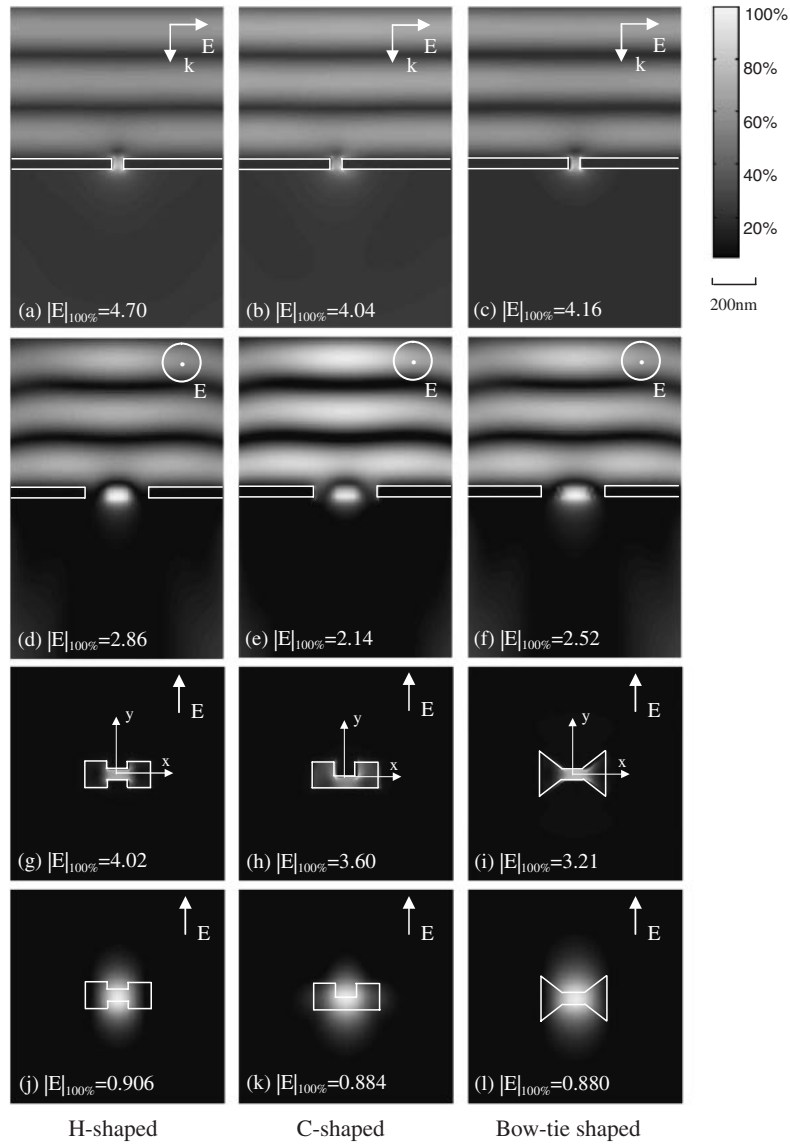
Fig. 13.   Distribution of the maximum electric field amplitude |E| of three different nano-apertures. From the first to third column, the aperture is 300×120 nm ($0.61 \times 0.25\lambda$) H-shaped with a 100×50 nm ($0.20 \times 0.10\lambda$) gap, 300×120 nm ($0.61 \times 0.25\lambda$) C-shaped with a 100×50 nm ($0.20 \times 0.10\lambda$) gap, and 300×200 nm ($0.61 \times 0.41\lambda$) bowtie-shaped with a 100×50 nm ($0.20 \times 0.10\lambda$) gap, respectively. From the first row to fourth row shows yz plane at $x = 0$, xz plane at $y = 0$, xy plane cutting through the middle of the film, and xy plane 50 nm (0.10λ) behind the apertures. An aluminum film of 50 nm (0.10λ) thick illuminated by y-polarized 488 nm incident light is considered for all cases. The peak amplitudes are shown as the insets of each plot. The amplitude of the incident electric field is 1.

12(c), 12(e)]. But the field intensity distribution of the C-shaped aperture on the yz plane at $x = 0$ is asymmetric due to the single ridge structure [Fig. 12(c)]. Only one peak is found on the xz plane at $y = 0$ for the H-shaped and bowtie-shaped apertures [Fig. 12(b), 12(f)], while two peaks can be observed at $d = 0$ for the C-shaped apertures [Fig. 12(d)]. The reason that the C-shaped aperture shows two peaks is because the xz plane at $y = 0$ intersects two corners of the aperture as can be seen in Fig. 13(h). There are some differences among the three ridged apertures in terms of output spot size and shape. At $d = 25$ nm (0.05λ), the smallest spot size is obtained from the H-shaped aperture. The transmitted field through the C-shaped aperture spreads out more rapidly along the x-direction than those through the other two apertures. In addition, due to the single ridge structure, the shape of the output spot is asymmetric for the C-shaped aperture along the y-direction, while the other two

keep a symmetric shape as shown in the fourth row in Fig. 13. However, it can be said that the difference among the electric field distributions of the three cases is small. Therefore, in practical applications, the choice of the shape depends only on convenience of fabrication. At present, all three types of apertures are being fabricated and the transmitted filed will be evaluated.

4.   Conclusions

We demonstrated that light spot with sub-wavelength resolution can be achieved through H-shaped or other ridged nano-apertures in a metal film while obtaining transmission efficiency above unity and high contrast compared with regular apertures. Using the waveguide cutoff analysis of the H-shaped aperture, it was shown that when it is operated in the optical frequency range between the cutoff frequencies of TE_{10} mode and TE_{20} mode, the fundamental TE_{10} mode is

excited and propagates through the aperture channel, which contributes to the high optical transmission efficiency. The small gap formed by the ridges plays a critical role to concentrate the light and determine the resolution. Fabry–Perot-like resonance was observed for the H-shaped aperture, and an optimal film thickness could be found for a particular operating wavelength to achieve even higher transmission. LSP is excited on the edges of the aperture in the silver film, which has a negative effect on the signal contrast and light concentration. In contrary, the LSP effect is weak in the aluminum film at the 488 nm incident wavelength. Further simulations and experiments will be conducted to optimize the nano-aperture design by considering the geometrical parameters, operating wavelength, and the type of metal to use.

Acknowledgement

1) E. H. Synge: Philos. Mag. **6** (1928) 356.
2) H. A. Bethe: Phys. Rev. **66** (1944) 163.
3) C. J. Bouwkamp: Philips Res. Rep. **5** (1950) 321.
4) Y. Leviatan: J. Appl. Phys. **60** (1986) 1577.
5) A. Roberts: J. Appl. Phys. **65** (1989) 2896.
6) K. Tanaka, T. Ohkubo, M. Oumi, Y. Mitsuoka, K. Nakajima, H. Hosaka and K. Itao: Jpn. J. Appl. Phys. **40** (2001) 1542.
7) X. Shi and L. Hesselink: Jpn. J. Appl. Phys. **41** (2002) 1632.
8) K. Tanaka, T. Ohkubo, M. Oumi, Y. Mitsuoka, K. Nakajima, H. Hosaka and K. Itao: Jpn. J. Appl. Phys. **41** (2002) 1628.
9) K. Sendur and W. Challener: J. Microscopy **210** (2003) 279.
10) K. Tanaka and M. Tanaka: J. Microscopy **210** (2003) 294.
11) K. S. Yee: IEEE Trans. Antennas Propagation **14** (1966) 302.
12) K. Kunz and R. Luebbers: *The Finite Difference Time Domain Method for Electromagnetics* (CRC Press, Boca Raton, 1996) p. 11, p. 123.
13) J. Liu, B. Xu and T. C. Chong: Jpn. J. Appl. Phys. **39** (2000) 687.
14) E. Vasilyeva and A. Taflove: *IEEE Antennas and Propagation Society, AP-S International Symposium* (IEEE, Piscataway, NJ, 1998) p. 1800.
15) O. J. F. Martin: J. Microscopy **194** (1999) 235.
16) M. Spajer, G. Parent, C. Bainier and D. Charraut: J. Microscopy **202** (2001) 45.
17) J. T. Krug, E. J. Sanchez and X. S. Xie: J. Chem. Phys. **116** (2002) 10895.
18) H. Nakamura, T. Sato, H. Kambe, K. Sawada and T. Saiki: J. Microscopy **202** (2001) 50.
19) P. N. Minh, T. Ono, S. Tanaka and M. Esashi: J. Microscopy **202** (2001) 28.
20) T. D. Milster, F. Akhavan, M. Bailey, J. K. Erwin and D. M. Felix: Jpn. J. Appl. Phys. **40** (2001) 1778.
21) S. Tang and T. D. Milster: Jpn. J. Appl. Phys. **42** (2003) 1090.
22) T. E. Schlesinger, T. Rausch, A. Itagi, J. Zhu, J. A. Bain and D. D. Stancil: Jpn. J. Appl. Phys. **41** (2002) 1821.
23) W. A. Challener, T. W. Mcdaniel, C. D. Mihalcea, K. R. Mountfield, K. Pelhos and I. K. Sendur: Jpn. J. Appl. Phys. **42** (2003) 981.
24) Z. P. Liao, H. L. Wong, G. P. Yang and Y. F. Yuan: Scientia Sinica **28** (1984) 1063.
25) Remcom Inc.: XFDTD 5.3 software (2002).
26) D. R. Lide: *CRC Handbook of Chemistry and Physics* (CRC Press, Roca Raton, 1996) 77th ed., Sect. 12, p. 12.
27) E. D. Palik: *Handbook of Optical Constants of Solids* (Academic, Orlando, 1985) Vol. 1, p. 350.
28) S. Ramo, J. R. Whinnery and T. V. Duzer: *Fields and Waves in Communication Electronics* (John Wiley & Sons, 1994) p. 396, p. 589.
29) J. Helszajn: *Ridge waveguides and passive microwave components* (IEE, London, 2000) p. 26.
30) S. Astilean, Ph. Lalanne and M. Palamaru: Opt. Commun. **175** (2000) 265.
31) Y. Takakura: Phy. Rev. Lett. **86** (2001) 5601.
32) C. L. Tan, Y. X. Yi and G. P. Wang: Acta Phys. Sinica **51** (2002) 1063.
33) H. Raether: *Surface Plasmons on Smooth and Rough Surfaces and on Gratings* (Springer, Berlin, 1988) p. 4.
34) T. W. Ebbesen, H. J. Lezec, H. F. Ghaemi, T. Thio and P. A. Wolff: Nature **391** (1998) 667.
35) H. F. Ghaemi, T. Thio, D. E. Grupp, T. W. Ebbesen and H. J. Lezec: Phys. Rev. B **58** (1998) 6779.